Examining layer height effects on the flexural and fracture response of plain and fiber-reinforced 3D-printed beams

Sooraj A. O. Nair¹, Avinaya Tripati¹, Narayanan Neithalath^{2,*}

Abstract

The development of concrete mixtures for digital manufacturing (3D printing), and evaluation of their rheological and mechanical properties, have received significant interest in recent years. However, for extrusion-based layered manufacturing, it is also important to select the appropriate printing parameters that have the potential to beneficially impact the performance of 3D printed elements. Among the many such parameters, this paper places emphasis on layer height, which has a direct bearing on rheology requirements, print quality, overall printing time, and interlayer bonding. Specifically, this paper examines the effects of layer height (as a function of the nozzle diameter) on the flexural strength and fracture properties of 3D printed beams. Flexural and fracture properties indicate that smaller layer heights are beneficial for unreinforced and fiber-reinforced 3D printed mortars, even though this results in greater number of interfaces and longer printing times. A small amount of steel fiber reinforcement is shown to be useful in eliminating the negative effects of weak interfaces on the measured bulk properties. Strain energy release rates, digital image correlation, and optical images/micrographs are used to explain crack propagation in layered 3D printed mortars under unnotched four-point, and notched three-point bending tests.

Keywords: 3D printing; Layer height; Fiber reinforcement; Fracture; Digital image correlation

¹ Graduate student, School of Sustainable Engineering and Built Environment, Arizona State University, Tempe AZ 85287

² Professor, School of Sustainable Engineering and Built Environment, Arizona State University, Tempe AZ 85287 *Corresponding author; e-mail: Narayanan.Neithalath@asu.edu

1 Introduction

Digital manufacturing or 3D printing is emerging as an effective technology to create multifunctional concrete elements [1–3] including those for habitation facilities, complex architectural needs, and in limited cases, structural members for infrastructural applications. Layer-by-layer extrusion of cementitious matrices is the most common mode of digital manufacturing of concrete elements and structures [1], even though other approaches including powder-bed fusion [4,5], injection 3D printing [6], and slip forming [7] are also being evaluated. From a materials standpoint, in addition to conventional cement-based mixtures, ultra-high performance concretes and other binder types such as alkali-activated ones are being explored for digital manufacturing [8–13]. Several studies in the recent past have comprehensively dealt with fresh characteristics of cementitious binders to ensure appropriate time-dependent rheological behavior including extrudability, shape-stability, and buildability [8,14–18], which are crucial towards successful 3D printing of concrete structures. Such studies, along with many ongoing research, are important since the fresh material properties influence the later-age properties of 3D printed concrete, perhaps more than those of conventional mold-cast concretes.

The mechanical properties, most notably the compressive and flexural strengths, are the basic parameters that are measured in order to design, specify, and aid in quality control of concrete for almost all applications. For 3D printed cement-based materials, while these are still considered to be the critical performance parameters, tensile, shear, and interlayer bond strengths are also important [19]. Because of the anisotropic nature of layered systems, mechanical properties are generally measured parallel and perpendicular to direction of printing [20]. The compressive strength is reported to be generally higher when tested perpendicular to the printing direction [9,21], although contrary results are also found [22]. The flexural strength is higher when tested perpendicular to the layering direction as compared to testing parallel to the layers, and generally lower than those of companion mold-cast specimens. This is typically attributed to weaker interfaces or the so-called cold-joints between printed layers, which also likely influences the durability of the 3D printed concrete elements through accelerated transport of water and other deteriorating agents. Weak interfaces and lower interlayer bond strengths result from a lack of adhesion due to inadequate rheological properties of the extruding material, the time gap between laying of the layers, interfacial voids, and drying; several of these aspects have been elucidated elsewhere [23–26]. In addition to the abovementioned factors, the printing parameters – layer height and width, the print velocity which defines the material flow rate and vertical printing rate for a given nozzle type (shape and dimensions), and the distance between the printing nozzle and the extruded layer (nozzle standoff distance), are also of significance [27–29]. For example, higher print time between layers and nozzle standoff distance are reported to result in reduced interlayer tensile strengths [27,28,30]. Several attempts at interface

strengthening also have been reported to overcome these deficiencies [31,32]. While some of these print parameters have been studied for their influence on mechanical properties in general, there is little reported work on the effects of these parameters on load-induced cracking, crack propagation, and failure of 3D printed concrete elements.

Among the several process parameters listed above that influence the properties, this study chooses to explore the influence of layer dimensions on the flexural and fracture response of plain and fiber-reinforced 3D printed beams. 3D printable mixtures, which has been shown to be satisfactory in terms of extrudability and buildability [33], are used. Other process parameters like printing speed, nozzle shape and diameter etc. are kept constant. The mixtures are moist-cured until the time of testing to ensure that drying does not cause undesirable interface defects that interfere with a proper analysis of the effects of layer dimensions on the properties. Tests are carried out perpendicular to the printing direction, on a series of beams extracted from 3D printed slabs. While the influence of metallic fiber reinforcement on the mechanical properties of 3D printed mixtures have been reported elsewhere [10,34–36], and fiber alignment shown to predominantly favor strengthening in the print direction [36], the combined influence of layer dimensions and fiber reinforcement needs to be better understood. The use of fibers longer than the nozzle size ensures a high degree of alignment of fibers [36]; however this paper specifically evaluates the effect of steel fibers that are smaller than the nozzle diameter, and smaller than or almost of the same size as the layer thickness, that helps avoid randomness in fiber distribution in the layers, on the load-induced crack propagation in layered materials. The results from this study are expected to shed more light on the influence of layer dimensions on flexural, fracture, and crack propagation response, to facilitate the choice of materials and process parameters for desirable properties.

2 Experimental Program

2.1 Materials and mixtures

The materials used in this study include a Type I Ordinary Portland Cement (OPC) conforming to ASTM C 150, fine limestone (L) powder conforming to ASTM C 568, and medium sand (M) conforming to ASTM C 778. The chemical and physical properties of the constituents are given in Table 1. The proportions of the printable mortars (plain and fiber-reinforced) containing 50% sand (by mass of the binder) are shown in Table 2. The water and admixture dosages were adjusted to ensure extrudability and buildability, as described in [8,15,33] (see Figure 1 also). Brass-coated straight steel fibers, 13 mm long and 0.20 mm in diameter (specific gravity of 6.8 g/cc), were used as fiber reinforcement. A polycarboxylate ether-based superplasticizer (0.20%-0.35% by mass of the binder) was used in all the mortar mixtures.

Table 1: Composition and properties of the mortar constituents

| Components of the binders | Chemical composition (% by mass) | | | | | | | | G G |
|---------------------------|----------------------------------|--------------------------------|--------------------------------|-------|------|--------|------|-------------------------|------|
| | SiO_2 | Al ₂ O ₃ | Fe ₂ O ₃ | CaO | MgO | SO_3 | LOI* | d ₅₀ (μm) | S.G |
| OPC | 19.60 | 4.09 | 3.39 | 63.21 | 3.37 | 3.17 | 2.54 | 11 | 3.15 |
| Limestone (L) | | | 1.5 | 2.70 | | | | | |
| Medium sand (M) | $SiO_2 > 99\%$ | | | | | | | | 2.40 |
| *Loss on ignition | | | | | | | | | |

Table 2: Mortar mixture proportions

| | Mass fraction of ingredients | | | | Water-to-powder | Superplasticizer ⁺ | |
|----------------------|------------------------------|------------------|-------------|---------------------|----------------------|-------------------------------|--|
| Mixture ID | OPC | Limestone (L) | Sand (M) | Steel Fiber (F)§ | ratio (w/p), by mass | (% by mass of binder) | |
| L ₃₀ -sM | 0.35 | 0.15 | 0.50 | | 0.35 | 0.25 | |
| L ₃₀ -sMF | 0.35 | 0.15 | 0.50 | 0.27 | 0.35 | 0.35 | |

^{*}Superplasticizer (indicated by 's') added at 0.25% by weight of powder

2.2 3D printing of mortars

The selected cement-based mortars shown in Table 2 were printed using a gantry printer with screw extruder system as shown in Figure 1(a). Figure 1(b) shows the extrudability and buildability of the chosen OPC-limestone mortar mixture. Mortar slabs 400 x 400 x 80 mm were printed at a print speed of 50 mm/s, and the stepper for the auger calibrated for a flow rate of 17 mL/s. A circular nozzle 20 mm in diameter (ND) was used to print filaments of a specified layer height (LH) and a fixed layer width (LW) of 22.5 mm (1.15 x ND). The print layer height was chosen as 0.25, 0.50, and 0.75 times that of the nozzle diameter, while keeping the print width and print speed constant, and a zero nozzle standoff distance. Layer heights smaller than ND are used so that the layer is pressed vertically when laid, to induce some transverse flow for filament overlap and thus eliminate defects. Companion specimens printed using layer heights larger than the nozzle diameter resulted in larger voids because of the absence of a vertical pressing force and improper filament overlap in the plane of printing. Figure 2 shows the schematic of different print parameters evaluated in this study. The mortar mixtures were 3D printed and moist-cured in a chamber at 23±2°C and > 98% RH for 28 days, after which the tests were carried out on beam specimens cut from the printed slabs (Figure 3).

[§]Percentage by volume of the mixture

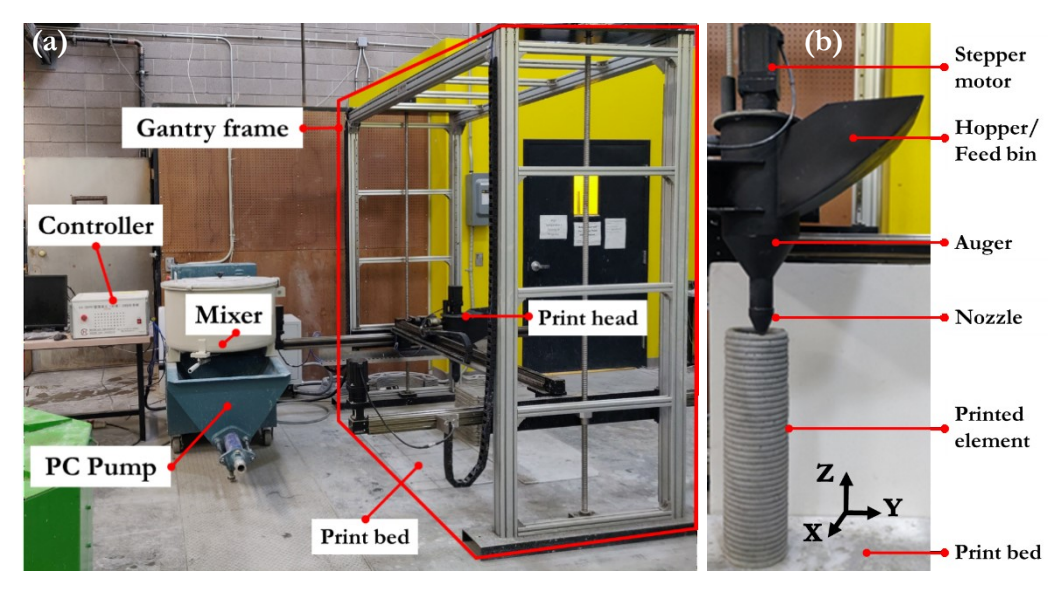


Figure 1: The 3D printing setup showing: (a) overall printer and controller setup, and (b) printing of a hollow column to evaluate extrudability and buildability. The eventual height of this column was 1.6 m.

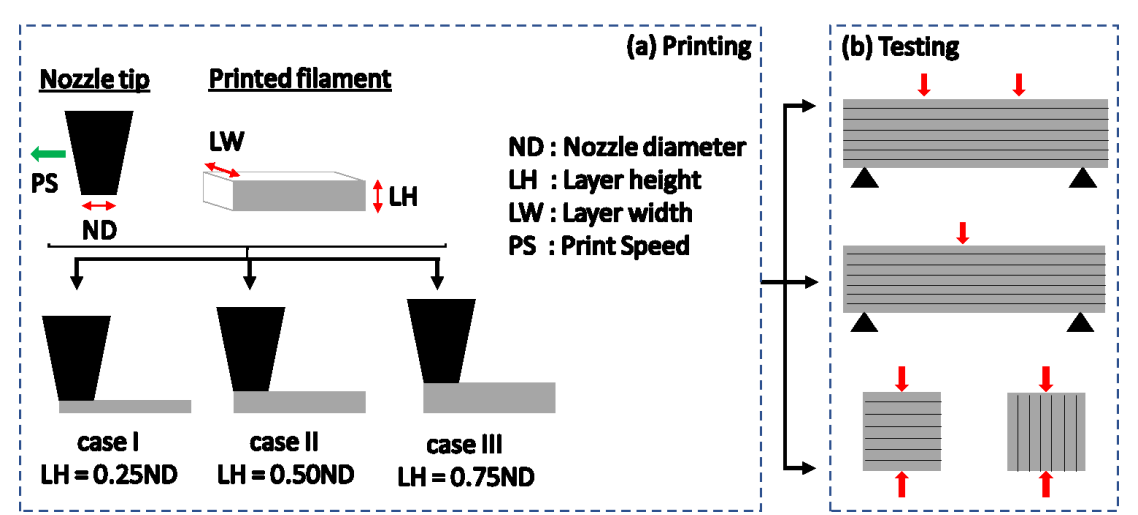


Figure 2: (a) Schematic showing the print cases with three different specimen types where the layer height (LH) of the system is varied as a ratio of the nozzle diameter (ND), and (b) the testing modes for flexure and compression. Only flexural tests are discussed in this paper.

2.3 Imaging of bulk and interface regions of the printed beams

Representative sections sliced from the printed slabs using a diamond-tipped saw were subjected to optical and scanning electron microscopy (SEM) to identify the differences in the bulk and interfacial regions of the printed material. Cross-sectional samples were extracted and first observed under an optical microscope (AMscope; 10-100X) to identify the material structure in the middle of the layers and at layer interfaces. SEM (SNE Plus 5400; 500-1000x) under secondary electron mode was used to evaluate the microstructural differences between the bulk and the interfaces in the plain and fiber-reinforced 3D printed mortars.

2.4 Flexural and fracture testing

The 3D printed slabs were cut into beams of 75 x 75 x 400 mm size for flexural testing after 28 days of moist curing. The printing process, printed specimens, and the cut specimens ready for either four-point testing or three-point notched beam testing are shown in Figure 3.



Figure 3: The 3D printed slab: (a) while printing, (b) after printing, and (c) after cutting into desired dimensions for testing.

The unnotched beams were tested under four-point bending as per ASTM C78/C78M-18 [37] to determine the flexural response. A servo-controlled universal testing machine (MTS 810) with a capacity of 100 kN was used. The four-point loading test was conducted using an effective span of 330 mm in monotonic displacement control, at a rate of 0.20 mm/min until failure. The notched beams were tested under threepoint bending [38] to determine the fracture toughness and critical crack tip opening displacement in accordance with the two-parameter fracture model (TPFM) [39,40]. The test was conducted in cyclic loading-and-unloading mode under crack mouth opening displacement (CMOD) control at a rate of 0.0004 mm/min. The beams had a 15 mm deep (1/5th of the depth of the beam) and 2 mm wide notch at the center, with an extensometer (gage length of 12.5 mm and maximum travel of 0.4 mm) mounted across the mouth of the notch. The first unloading was done at approximately 95% of the peak load (P_{max}) which corresponds to a crack opening displacement of about 0.032 mm. Thereafter, the unloading and reloading cycles were repeated at every 0.032 mm step until a total CMOD of 0.20 mm was reached or the specimen failed, whichever happened first. The unloading compliance was used to estimate the fracture parameters based on TPFM [40,41]. The loading compliance (C_i) was used to calculate the Young's modulus (E) and the critical crack length (ac). The critical strain energy release rate (GR) was also calculated based on the resistance curve (R-curve) approach [42–44]. The strain energy rate required for crack propagation is an increasing and convex function for quasi-brittle materials such as concrete, and is the sum of both the elastic and inelastic strain energies. The former, corresponding to energy release rate due to incremental crack growth, was determined from the unloading compliance, while the latter, corresponding to non-linear effects caused due to crack opening, was obtained from the inelastic CMOD [41].

2.5 Digital image correlation for visualizing strain fields and crack propagation

Digital image correlation (DIC), which is a non-contact means to acquire the surface strain fields in the specimen during the testing, was also carried out along with flexural and fracture testing. The DIC data was used to identify and track crack initiation and propagation, and to extract the true displacement of the specimen. The DIC setup (Figure 4a) includes two cameras focused on a speckled area of interest on the beam, which is illuminated by high-intensity flood lights. The aperture and focus were adjusted such that the speckle pattern could be tracked across images taken by the cameras during the testing. The data acquisition (DAQ) unit controls the cameras and the frequency of image capture (typically 1 Hz). The time-stamped load-displacement data and the DIC data were synchronized to extract the corrected load-deflection curves. Figure 4b and Figure 4c show the typical DIC strain fields after post-processing of the images for beams subjected to four-point bending (unnotched) and three-point bending (notched), respectively. The process of using surface displacement fields obtained from DIC to obtain the components of Lagrangian strain fields have been described in detail elsewhere [45,46].

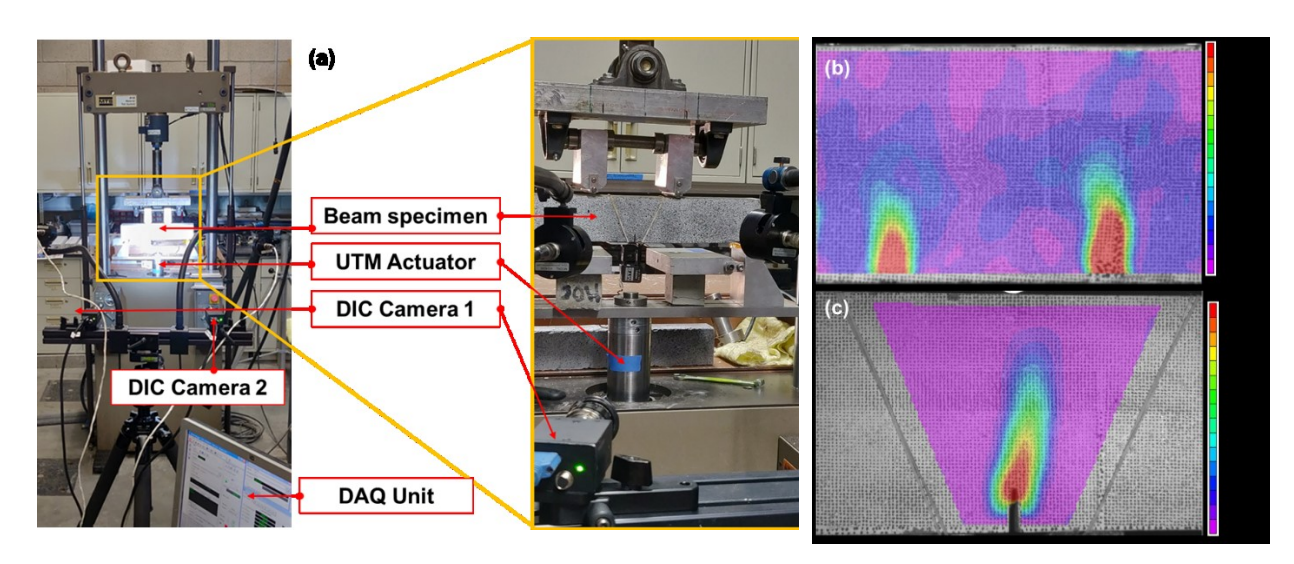


Figure 4: Flexure test showing: (a) DIC setup and its components, (b) visualization of localized strains in unnotched four-point loading, and (c) notched three-point loading.

3 Results and Discussions

3.1 Analysis of bulk and interface regions in layered mortars

3.1.1 Inferences from optical images

Optical microscopy was used to determine the effects of layer height on the hardened printed material structure. Figure 5(a-c) show typical cross-sections of the plain (unreinforced) mortar specimen (L_{30} -sM)

printed using different layer heights. The images shown are transverse to the filament, i.e., transverse to the direction of printing. It is evident that the void content in the printed plain mortar increases with layer height for the mixture and printing parameters chosen. For the specimen with the lowest layer height (5 mm; LH5), relatively fewer, smaller voids are visible in the optical image. It is likely that the pressure applied by the print head to achieve the smaller layer height could have resulted in reduced voids in this case. In the LH10 and LH15 specimens (10 mm and 15 mm layer height), the larger voids are found to be somewhat ordered, and located where the filaments overlap in the horizontal and vertical directions. The flow rate was slightly adjusted to reduce the possibility of occurrence of voids between the overlapping filaments. However, with increasing layer height, it is noticed that the discontinuities at the filament edges, observable through optimal microscopy, increase, an observation made in [47] as well. A layer height of 15 mm, which is 0.75 times the nozzle diameter, results in faster printing and increased output, but contains imperfections as shown in these figures. Selecting an optimal layer height can aid in optimizing the vertical print rate since a layer height of 5 mm would take almost three times the print time when compared to a layer height of 15 mm. In cases where the print path is longer, this could also result in the drying of the printed layer before the next layer could be laid on top, increasing the likely incidence of interfacial defects.

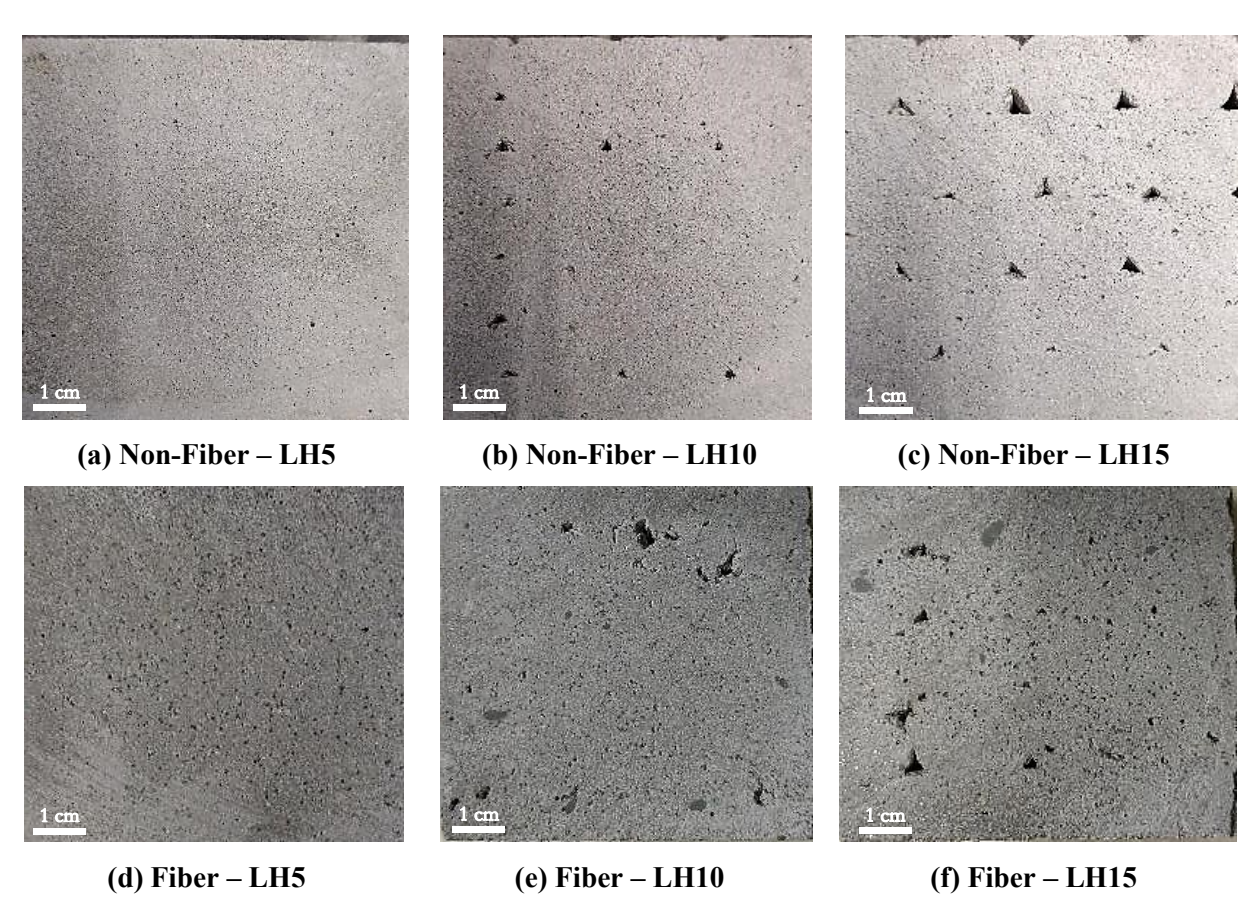


Figure 5: Optical images of beam cross-section showing the typical void distribution for different cases of layer heights in plain and steel fiber-reinforced mortars.

To improve the mechanical properties of the printed structure, 13 mm long steel fibers were used to modify the mortars, and the mixture consistency was adjusted through the superplasticizer content. The fiber length is 0.65 times the nozzle diameter, and almost equal to or larger than the layer heights, depending on the layer height used. Note that a fiber length much smaller than the nozzle diameter and layer height could result in a random orientation of the fibers in the layer. Similar trends in void content with layer height as noticed for the unreinforced mortar are also valid for the fiber-reinforced mortars shown in Figure 5(d-f). As shown in Table 2, a higher amount of superplasticizer was used for the fiber-reinforced mortar, and the consequent improved consistency resulted in a reduction in the amount of voids between overlapping filaments, showing that mixture modification could be beneficial in reducing the macroscale inhomogeneities at the interfaces. However, the LH5 fiber-reinforced mixture showed a relatively higher void content when compared to the companion unreinforced mortar. This can be attributed to the fiber length being > 2 times the layer height in this case, resulting in the fibers scratching the surface of the printed layers during the layered printing process. This effect is rather negligible for the LH10 and LH15 cases, since the fibers are found to be reasonably contained within the layers, as illustrated later.

3.1.2 Layer interfaces in plain and fiber-reinforced mortars

The layer interfaces were examined in detail using SEM. The LH5 specimens are used here since optical images showed that visible voids exist at the interfaces for the LH10 and LH15 cases, and SEM investigation is not necessary. Micropores are observed in the vicinity of layer interface (marked by the dotted line) as shown in Figure 6, but overall, the interface is rather dense. Unlike the LH10 and LH15 cases where pores near the layer interfaces are easily visible in optical images, the plain LH5 mixture shows much smaller pores (Figure 6a) in the layer interface. Figure 6b shows the layer interface in the LH5 fiberreinforced mortar. Since fibers are likely to be generally oriented along the layering direction in 3D printed systems, especially when the layer height is equal to or slightly larger than the fiber length as is the case here, the fibers can be expected to resist crack opening and provide post-peak stiffness to the specimens. However, for layer heights that are lower than the fiber length, a weak fiber-to-matrix interface is observed in some cases as shown in Figure 6b, even though some fibers are bonded strongly to the matrix. Here, for the LH5 specimen, two fibers (marked by the red arrows) and the weaker interface around them are shown, likely due to the fiber length-layer height incompatibility, as mentioned earlier. This influences the flexural performance as will be discussed in a forthcoming section. Figure 6c shows a close up at a layer interface marked with the dotted line, around which voids are also present. Additionally, microcracks are visible in the interfacial region as shown in Figure 6d. Figure 6e shows the fiber-matrix interface where a fiber embedded in the matrix in the direction normal to those in Figure 6c and d is shown, demonstrating the fiber-matrix interface effects, especially near the layer interface.

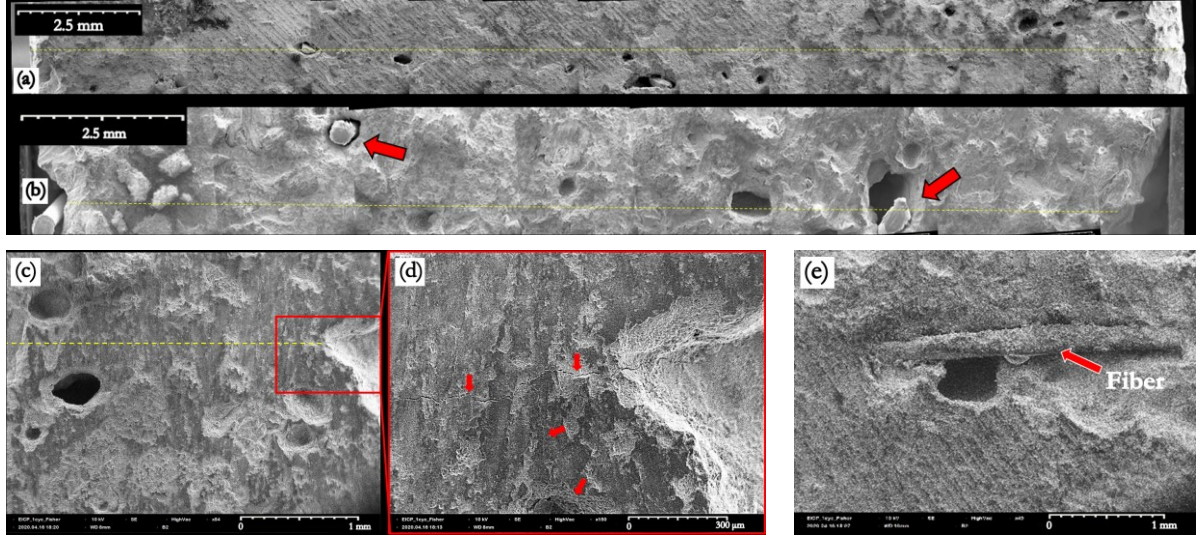


Figure 6: SEM images stitched in the vicinity of a typical layer interface in: (a) unreinforced specimen, and (b) fiber-reinforced specimens, with a LH of 5 mm, (c) pores near the interface in a fiber specimen with LH of 5 mm, (d) a close up of the interfacial region showing micro-cracks between the layers, and (e) weak bond between the fiber and an interface along with voids in the vicinity.

3.2 Effect of layer height on flexural strength

3D printed beams with different layer heights, extracted from slabs, were subjected to four-point bending tests. For the unreinforced mortar specimens, a sudden and brittle failure occurred, as expected. The flexural strength of the 3D printed mixtures shown in Figure 7 are lower than those reported for similar mold-cast mortars [41]. Similar results are reported elsewhere [26,48]. Note that the compressive strength does not show significant layering effects as noted from our companion work and other reported publications [22,28]. The peak flexural strength was found to be higher for a smaller layer height, for the unreinforced mortars as shown in Figure 7. This can be attributed to the increase in porosity both at the layer interfaces as well as where the adjacent filaments overlap, for higher LH cases as shown earlier. Moreover, the vertical force exerted during extrusion in the case of lower layer heights results in enhanced consolidation of the layer. It has been shown that decreasing layer height below 10 mm allows the pressing force exerted by the nozzle to be dominant than the overburden pressure [49]. This was established in this study by printing a typical filament on a sensitive weighing balance, which showed that the pressing force was ~50% lower when the layer height was increased from 5 mm to 15 mm, while maintaining other print parameters the same. This vertical extrusion force could be beneficial since it is more likely to strengthen the bulk layer and the interfaces, as opposed to printing with a non-zero nozzle standoff distance. However, this could also be detrimental to the buildability of the structure if the binder is soft (low yield stress to flow onset) or the structural stiffness is low (causing buckling under eccentric loading). These aspects are important in 3D

printing, and further reinforces the idea that fresh properties of 3D printable mortars are even more significant to the hardened response, than in the case of conventional mold-cast concretes.

The fiber-reinforced mortars demonstrate higher flexural strengths when the layer height is higher. The average flexural strength increases by 30-60% when fibers are incorporated; the larger the LH, the more the difference between the strengths of plain and fiber-reinforced mortars, within the range of parameters studied here. The effects of incorporated voids at the interface at higher layer heights (Figure 5) are somewhat compensated by the presence of fibers, where fewer number of interfaces are observed to result in somewhat higher strengths. The variability in flexural strengths also tends to be lower for higher LH, which can be attributed to the reduced number of layer interfaces in such cases. Overall, the flexural strength results indicate that a small volume of fibers is beneficial in enhancing the properties of 3D printed mixtures and helps overcome some of the layering-induced adverse effects with respect to strength.

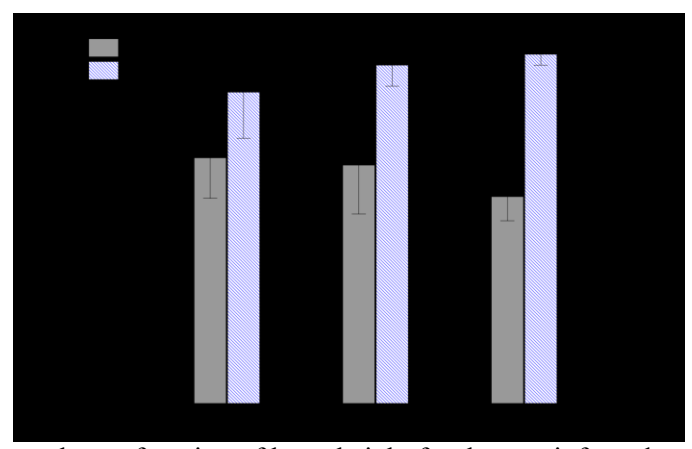


Figure 7: Flexural strength as a function of layer height for the unreinforced and fiber-reinforced 3D printed mortars. The error bars indicate one standard deviation of strengths based on 3-5 specimens tested.

As shown in Figure 7, an increase in layer height results in a slight increase in the flexural strengths for fiber-reinforced mortars, even though demonstrable increase in porosity was shown earlier, with increasing layer height. However, the possibility of longer fibers creating defects in the printed structure are also higher when LH is lower than the fiber length. This is illustrated in Figure 8 (drawn to scale). In specimens printed with lower layer heights (e.g., LH5), the fibers being longer than the layer height, are not always constrained within the layer, and they scratch the surface and creates defects, which were clearly observed during the printing process. The fibers that project out from the layer (as shown in Figure 8) for smaller LH cases are further disturbed when the following layer is printed, resulting in layer defects, which negates some of the beneficial effects of fiber addition. Since no vibration or consolidation, as in the case of conventional concrete, happens here, these fresh-state defects are not completely eliminated with time, and thus, influences the hardened state properties. As the layer height increases, fibers have more flexibility in

aligning within the layer, while being laid through the nozzle. This effect of better fiber alignment and placement eliminates some of the interfacial defects (even though reduced nozzle pressing force results in lower layer compaction), resulting in a slightly better flexural response for the specimens with higher layer heights. Thus, as noticed in Figure 7, the difference between the flexural strengths of unreinforced and fiber-reinforced 3D printed mortars increases when the LH increases. The poor matrix-fiber interface (sometimes, a result of lack of consolidation) also could contribute to the reduced flexural strengths [50]. Though fibers larger than the nozzle size is better to ensure fiber alignment [36], it is shown here that the layer height also needs to be in the range of fiber length to ensure proper alignment, especially for stiffer fibers like steel fibers. The use of fibers much smaller than the layer height potentially eliminates the layer defect issues reported here, but the fibers are likely to be randomly aligned in such a case. The use of randomly aligned elongated metallic particulates [45] as matrix reinforcement in 3D printed mortars (not shown in this study) was found to result in only slight improvements in flexural strengths, even though the toughness was observed to increase, as expected.

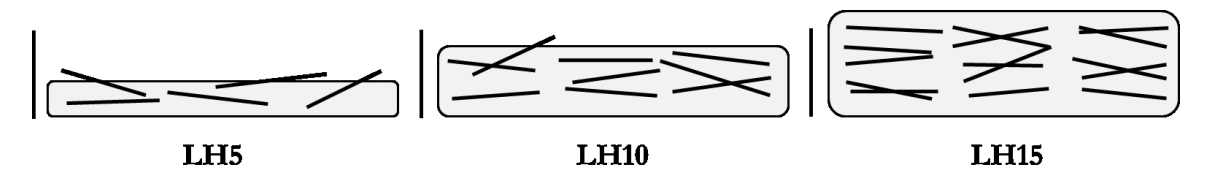


Figure 8: Illustration of fiber orientation with layer height, showing increasing degree of freedom for fiber orientation with increasing layer height. The drawing is scaled proportional to the actual dimensions, and includes a fiber placed to the left of each LH case for comparison.

3.3 Crack propagation under four-point bending using DIC

DIC analysis of typical unreinforced and fiber-reinforced specimens under four-point bending is shown in Figure 13. The strain fields were evaluated from the displacement fields determined from DIC. Note the difference in the magnitude of Lagrangian strains in both the specimen types, with the fiber-reinforced specimens demonstrating much higher strain capacities in the peak and post-peak regions.

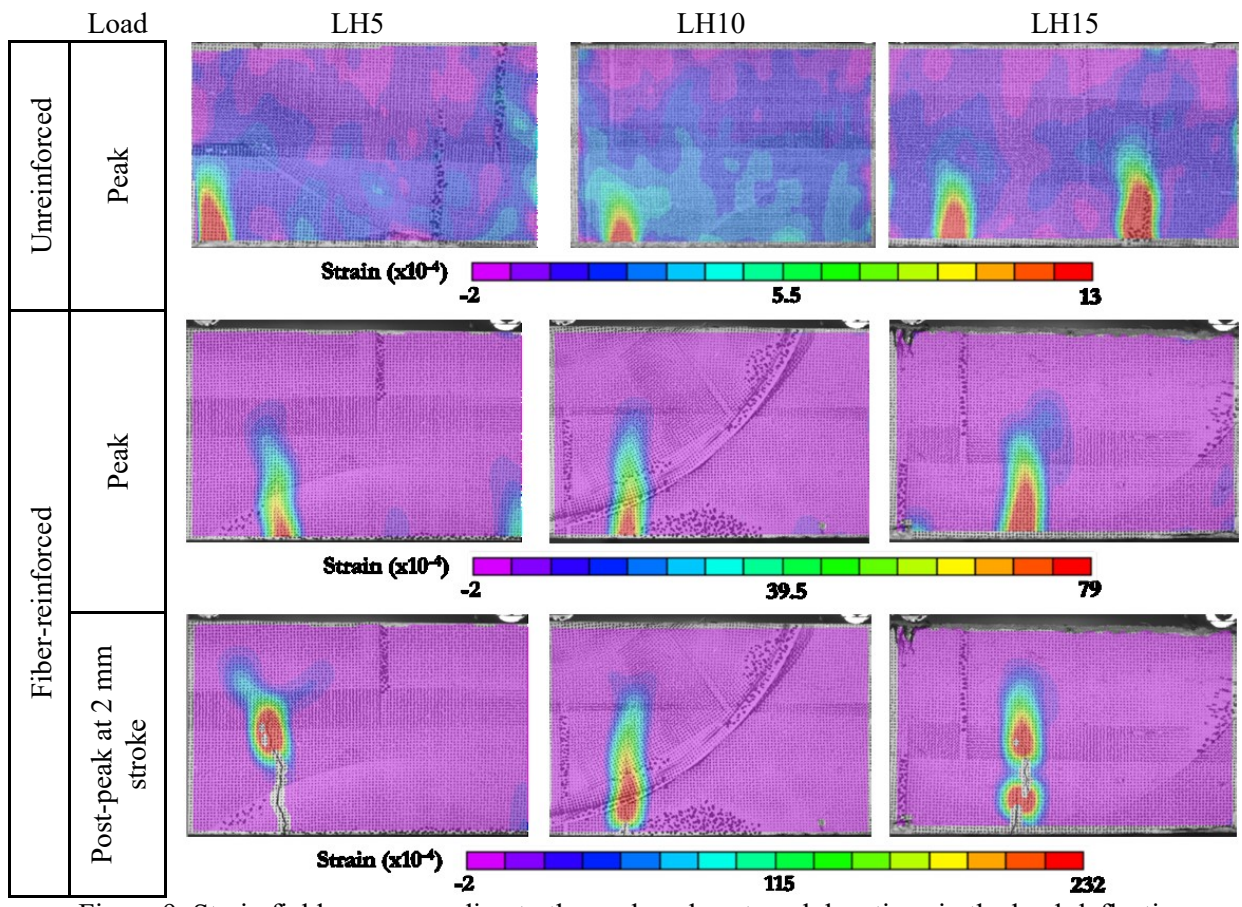


Figure 9: Strain fields corresponding to the peak and post-peak locations in the load-deflection response under four-point bending.

The strain fields are shown at the peak load only for the unreinforced specimens since there is little localization before the peak, and there is no discernible post-peak region. At the peak load, strain localization, in general, tends to be more prominent at higher layer heights. The enhanced energy dissipation because of the larger number of layer interfaces in the LH5 case likely results in lower strains. For the fiber-reinforced specimens, at the peak load, the crack starts to initiate with strains at the crack tip around 6 times higher than those in the unreinforced specimens at the corresponding peak load. In the post-peak response, the condition of the specimen at a vertical displacement of 2 mm is shown, where the crack has propagated much further. The localized strains near the crack tip is about 4 times of the value at the peak. Figure 10 shows the propagation of the main crack and its directionality near the interfacial regions in typical unreinforced and fiber-reinforced mixtures (LH15 case is shown here). The images correspond to the point close to the peak stress for the unreinforced specimen, and post-peak at a midspan deflection of about 1.5 mm for the fiber-reinforced specimen. The horizontal dotted lines show the layer interfaces and the arrows indicate how the layer interface results in a deviation in the crack direction along its path. A similar

mechanism also exists in the LH5 and LH10 cases, but is more obvious for the LH15 case because of the higher layer height.

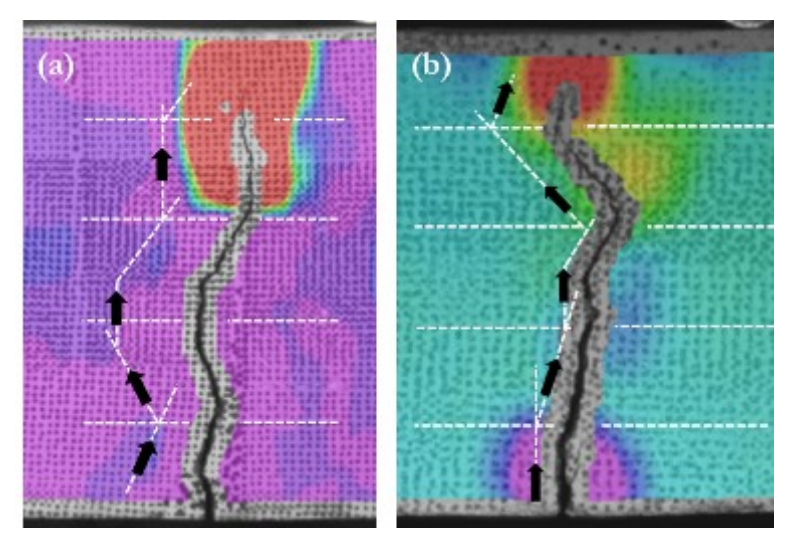


Figure 10: The crack path showing crack deviation at layer interfaces in: (a) an unreinforced, and (b) fiber-reinforced specimen. The interface is denoted by the horizontal dotted lines and the change in direction near the interface indicated by the arrows.

3.4 Effect of layer height on fracture response

3.4.1 Fracture parameters

Typical results of three-point cyclic bending tests on notched beams are shown in Figure 11a and b for the unreinforced and fiber-reinforced specimens, printed using different layer heights. The fiber-reinforced specimens demonstrate higher peak loads, and higher stiffnesses in the pre-peak elastic and post-peak regions, attributed to the presence of stiffer fibers and associated crack bridging. The layering of fibers along the horizontal direction, shown in Figure 8, perpendicular to the direction of cracking, lends these systems enhanced crack resistance and multiple-cycle load capacity as shown in Figure 11b. In general, the unreinforced specimens demonstrate a reduction in load capacity as the layer height increases (similar to Figure 7), while the difference is found to be insignificant for the fiber-reinforced specimens. A closer look at the unloading compliance also shows that an increase in layer height makes the unreinforced specimens more compliant in the post-peak region. In contrast, the fiber-reinforced specimens tend to show a strain hardening behavior near the peak when crack initiates, and the capacity reduction from peak to the chosen CMOD maximum (about 0.20 mm) was only around 20% due to the influence of fibers. The unreinforced specimens show a significant decrease in the post-peak load when compared to the fiber-reinforced specimens, as expected.

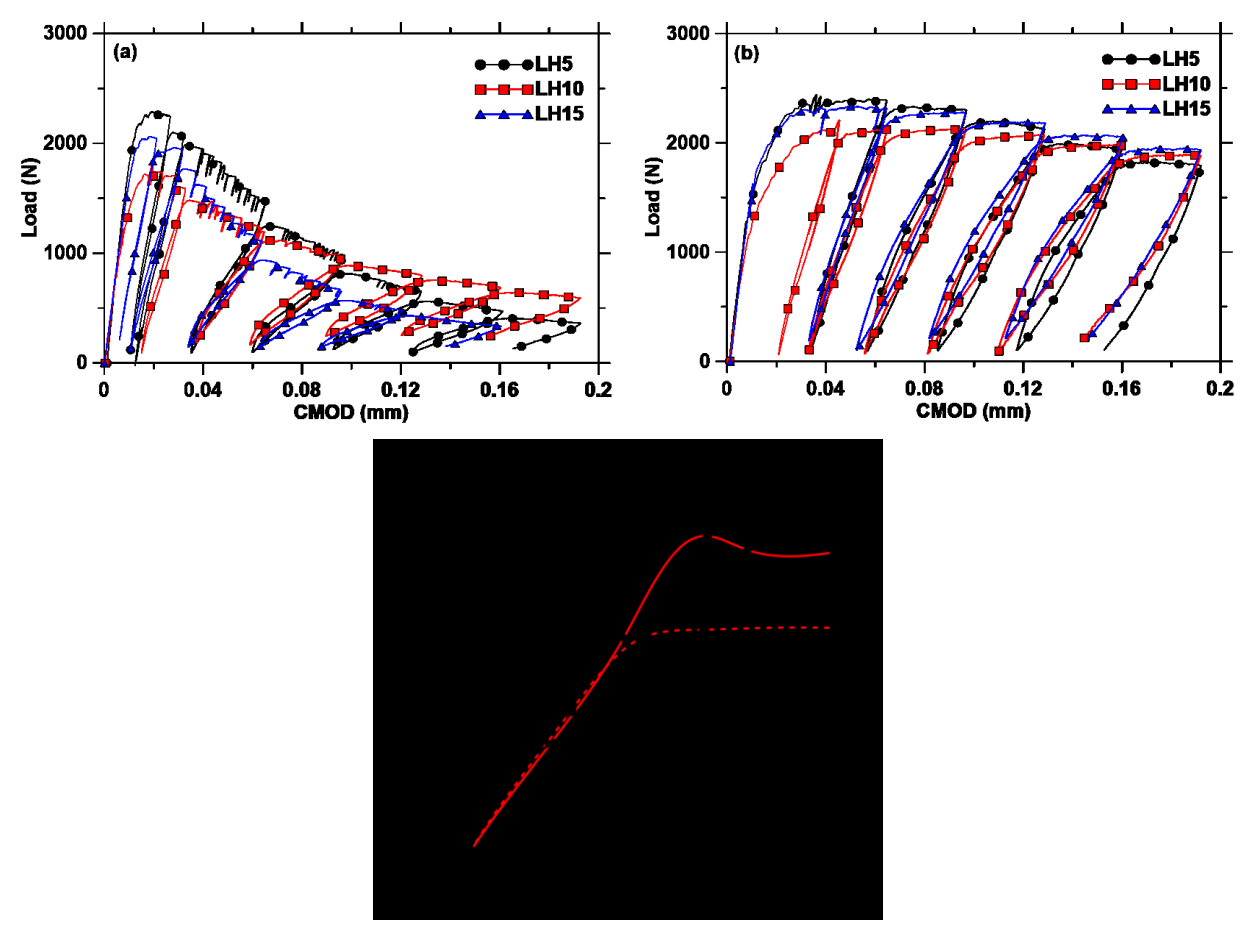


Figure 11: Cyclic CMOD-controlled three-point bending test results for: (a) unreinforced, (b) fiber-reinforced specimens, as a function of layer height, and (c) strain energy release rate as a function of crack extension.

Figure 11c shows the R-curves for the unreinforced and fiber-reinforced mortars printed using two layer heights. The R-curves show an initial rising region where the resistance increases with crack length, denoting the formation of a process zone, and a strain energy plateau denoting steady-state crack propagation. The transition between these two regions, and the value of the strain energy plateau (G_{R-max}), is seen to be dependent on the layer height and the presence of fibers. Past studies have explored the relative contributions of elastic and inelastic components of G_R , with an emphasis on the contributions of matrix modifications and/or fiber reinforcement to energy release rates [41,51].

The fracture parameters calculated using TPFM are plotted in Figure 12a and b. An elastically equivalent fracture toughness, K_{IC} , is an important parameter in the fracture characterization of cementitious systems. The calculated Mode-I fracture toughness, K_{IC} , and the critical crack tip opening displacement, CTOD_c, are similar to or slightly lower than those reported for mold-cast conventional unreinforced limestone-containing mortars of similar composition [41]. For instance, the mold-cast specimens show a K_{IC} around 25 MPa-mm^{0.5} while the 3D printed specimens show K_{IC} values between 20 and 24 MPa-mm^{0.5}. This slight

reduction in K_{IC} could be attributed to the lack of compaction and the presence of defects during the printing process. In general, K_{IC} shows marginal decrease with increasing layer height for both the unreinforced and fiber-reinforced mixtures. This is probably attributed to the fact that higher number of layer interfaces could result in more energy dissipation during crack propagation, in addition to the crack path tortuosity. The average CTOD_c values are practically invariant with layer height; the layering effect, within the range of the parameters studied here, does not alter the limit beyond which unstable crack propagation begins. Fiber-reinforced specimens show K_{IC} and CTOD_c values that are higher by almost 30% when compared to the unreinforced specimens, which can be attributed to crack arresting and fiber bridging in the crack wake [52]. The relatively minor effect of the selected layer height range on fracture toughness and CTOD_c demonstrates that a higher layer height that enables faster printing process can be chosen without compromising the fracture properties. This was also shown with the flexural strength for the fiber-reinforced mixtures, while for the unreinforced mixtures, increasing layer height did cause a small but noticeable reduction in strength.

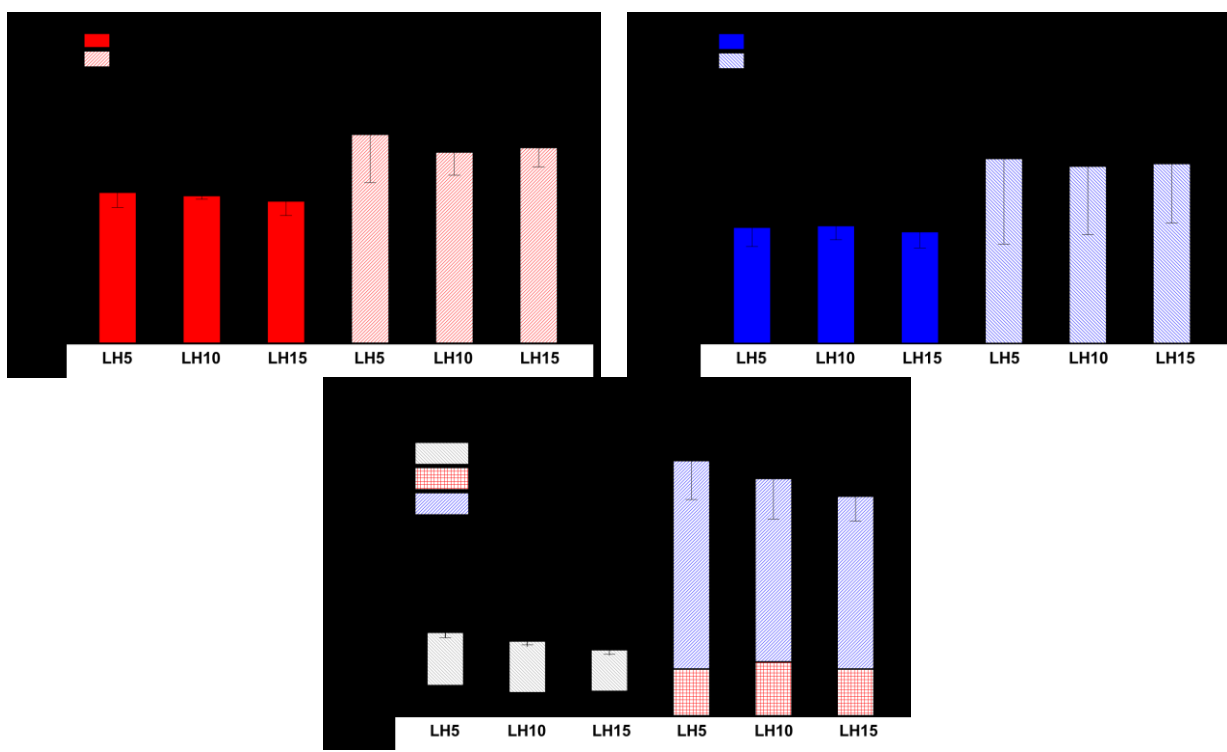


Figure 12: The variation of: (a) fracture toughness, K_{IC}, (b) critical crack tip opening displacement, CTOD_c, and (c) strain energy release rate plateau (G_{R-max}), with layer height for unreinforced and reinforced 3D printed specimens, showing the contributions of the elastic (G_e) and inelastic (G_{ie}) components. The error bars indicate one standard deviation of the properties based on 3-5 specimens tested.

The strain energy release rate plateau, G_{R-max}, is shown in Figure 12c, along with the relative contributions of the elastic and inelastic components. This was extracted from data corresponding to several loading-

unloading cycles of the closed-loop CMOD-controlled testing, under the assumption that stable crack propagation leads to an increase in compliance. The G_{R-max} for unreinforced printed specimens are rather similar to that of mold-cast specimens (a value of ~ 0.03 -0.04 N/mm [41]). G_{R-max} is higher for specimens printed using smaller layer heights; there are more interfaces that likely act as crack barriers. The fiber-reinforced mortars show a G_{R-max} that is 3 times higher than those of the unreinforced specimens, owing to the presence of fibers that bridge the matrix while resisting fracture. For both cases, it is also noticeable that a larger number of interfaces (smaller LH) results in an increase in the inelastic component of the strain energy, with the elastic component remaining roughly similar for all the layer heights studied. A much larger difference between elastic and inelastic components is noticed for the fiber-reinforced mortars. The synergistic effect of fibers, which are known to enhance the inelastic strain energy release [51], and the influence of layers is noted here. Even considering the interlayer defects introduced by fibers that are longer than the layer height, the overall fracture response is better when the layer height is smaller.

The tendency for crack propagation in layered systems involve two different fracture energies: for crack penetration across the interface (G_p), and for crack deflection along the interface (G_d). It is known that crack penetrates across the interface if the ratio G_{f-interface}/G_{f-layer} is greater than the ratio G_d/G_p. Considering that the interface will be slightly more compliant# than the bulk (due to defects), and that crack extension towards a more compliant region results in greater release of energy [53], one can deduce that G_p > G_d, thus favoring crack penetration into the interface and to the next layer, as observed in Figure 10, albeit with a minor change in the angle of propagation. If the interfaces were very weak, then the fracture of first layer would be followed by crack propagation along the interface, after which the crack could still deviate into the bulk when $G_d \le G_p$, as is the case for step-like fracture reported in laminated ceramics and composites [53] (see Figure 13, for a notched three-point bending specimen). Additionally, the elastic property gradient at the crack front dictates the crack propagation direction, as has been shown for layered ceramics [53]. Even though the interfacial region is generally a little more complaint than the bulk in 3D printed mortars, the elastic property mismatch between the layer and interface can be taken to be rather small, especially for lower LH cases where the pressing force exerted by the nozzle consolidates the layer and the interface. Thus, in most of the cases evaluated here, it is energetically more favorable for the crack to grow across the interface. The interfaces in the specimens studied, in general, were not thick enough or weak enough to promote an alternate failure mechanism.

[#] It needs to be mentioned that interface mechanical characterization (e.g., using nanoindentation) has not been carried out in this work to quantify the reduction in elastic properties as compared to the bulk; however it is seen from this work and several other studies, that the layer interface is more porous [24,27–30,47], from which some elastic property reduction can be easily inferred.

Figure 13 shows optical images of crack propagation patterns typically observed for the different layer height cases in unreinforced mortars under notched three-point bending. For low LH cases, e.g., LH5 and LH10, Figure 13a and b show that the cracks cross the layer interface (denoted by the dotted lines) and exhibit some branching because of energy dissipation in the interface. The branching could also be an artifact of the loading-unloading cycles adopted in the notched three-point bending testing. For the high LH case, as shown in Figure 5, the interface is rather weak, and some crack deflection along the interface is observed for some of the cracks, the reasons for which were explained earlier [53]. Such crack deflection is not observed for the fiber-reinforced specimen with larger LH, owing to the fiber bridging that arrests the crack movement, dissipates energy, and avoids meandering of the crack along the interface. Crack deflection is also not noticed in the four-point test (Figure 10) because of the faster loading rate, which results in rapid crack opening, and therefore the propagation energy (G_p) exceeding the deflection energy (G_d) at all times.

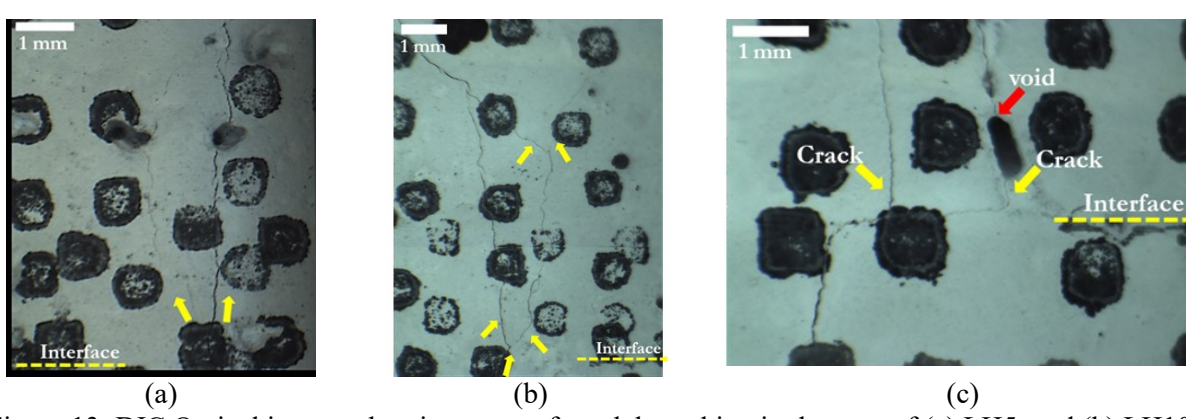


Figure 13: DIC Optical images showing cases of crack branching in the case of (a) LH5, and (b) LH10, (c) crack deflection along an interface in LH15. The black circles are speckles for DIC.

3.4.2 Crack extension and strain profiles using DIC

The microcracked, inelastic region around the traction-free crack tip in concrete is generally termed as the fracture process zone (FPZ). The fracture energy is related to the size of the FPZ [45,46]. The localization of strain above the notch as the CMOD increases during fracture, is shown in Figure 14 and 15 for the mortars printed using different layer heights. The spread of FPZ in the direction of crack extension increases as the CMOD is increased. The magnitude of the localized strains also increases in part due to the increasing CMOD. It is noticed that the localized zone at the tip of the crack makes its appearance before the peak load is reached. The FPZ becomes prominent when the peak load is reached and then it grows in a stable manner in the post-peak zone as the CMOD increases. The localized zone spreads rapidly in the post-peak zone.

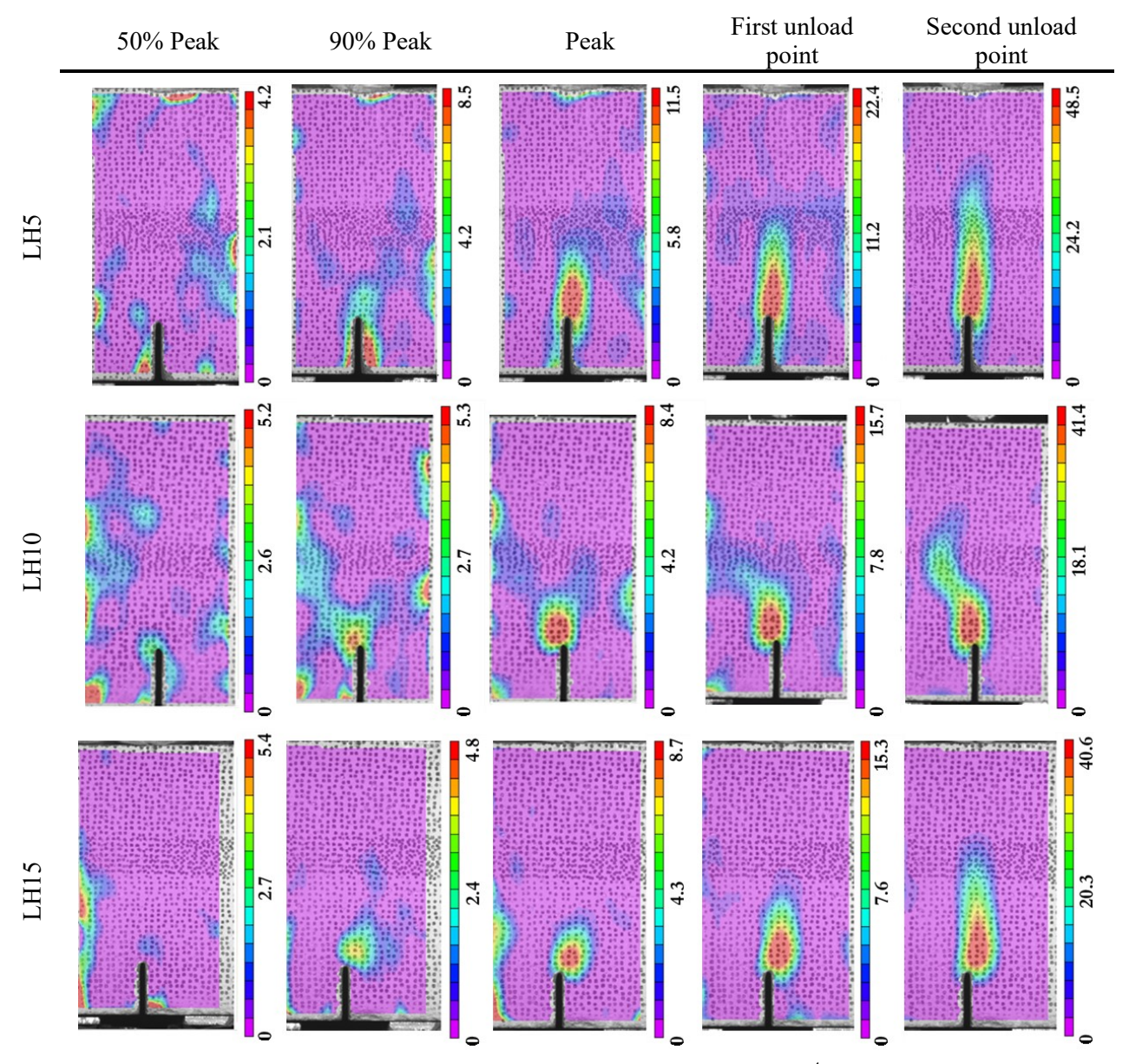


Figure 14: DIC images showing strain localization (principal strains $\varepsilon_{xx} \times 10^{-4}$) for unreinforced notched beams under three-point bending.

Figure 14 shows the strain profiles at the tip of the notch for the unreinforced mortars, at different locations in the cyclic load-CMOD curve, which helps to visualize the surface strain profiles as a function of the layer height and the load. It is generally observed that the FPZ at the peak is sharper and well-formed for the LH5 case, in line with the higher fracture energy shown in Figure 12. With increasing layer height, the process zone length at the peak load reduces. This effect is predominant at the first unload point as well, where the crack front has progressed further in the LH5 specimen than the LH10 and LH15 cases, which feature more compliant interfaces (i.e., because of increased porosity). Additionally, the critical crack length (a_c) calculated is in the range of 23-27 mm for the unreinforced mortars, which corresponds to a

crack extension of 8-12 mm (accounting for the initial notch length, $a_0 = 15$ mm). This indicates that there are at least one or two layer interfaces within the critical crack length itself for LH5 and LH10 cases, while no interfaces exist for the LH15 case. This helps in larger energy dissipation due to the slightly more compliant interfaces and increases the fracture energy release rate. The strain profiles at the tip of the notch for the fiber-reinforced specimens are shown in Figure 15. At, and beyond the peak load, the layer height seems to be less influential as can be noticed from these images, showing the dominant influence of fibers over layer height, in strain localization and crack propagation.

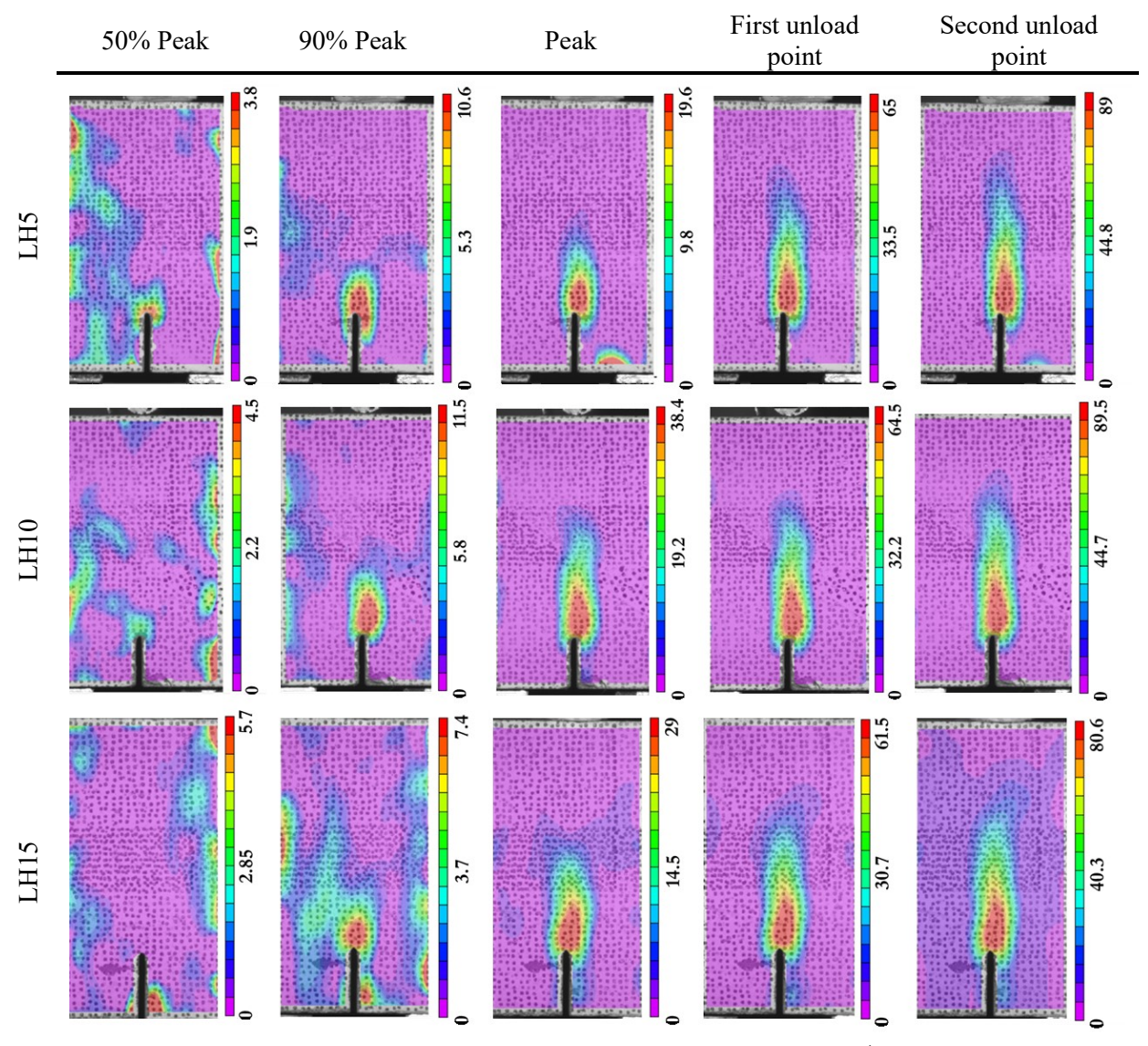


Figure 15: DIC images showing strain localization (principal strains $\varepsilon_{xx} \times 10^{-4}$) for fiber-reinforced notched beams under three-point bending.

Figure 16 shows the load-crack extension and CTOD-crack extension relationships for the LH5 and LH15 specimens for unreinforced and fiber-reinforced cases. The crack extension was determined based on the effective crack length corresponding to each point in the load-CMOD relationship as explained in [41,54].

The difference in behavior between the unreinforced and fiber-reinforced specimens can be clearly identified from this figure, while the layer effects (between LH5 and LH15 cases) are almost negligible. Figure 16a shows that, for a given crack extension, the LH5 specimen carries slightly more load than LH15 specimen in the initial pre-peak region, consistent with the flexural strength data. The fiber-reinforced specimens show higher loads at much higher crack extensions. The fibers bridge the crack, and the crack opening results in energy dissipation which is reflected in the form of increased inelastic strain energy with increasing crack extension as shown in Figure 12c. The change in CTOD with crack extension is shown in Figure 16b, with the location of CTOD_c values in the curves shown by the dotted lines. The crack propagation is stable until the dotted line (pre-critical to the left; CTOD < CTOD_c) while unstable propagation occurs beyond this line (post-critical to the right; CTOD > CTOD_c). The lower layer height specimens (i.e. LH5) show higher crack extensions at the corresponding CTOD_c values for the unreinforced and fiber-reinforced cases, in line with the strain energy release rates shown earlier. This can also be ascertained from the DIC images corresponding to the post-peak regions shown in Figure 14 and Figure 15.

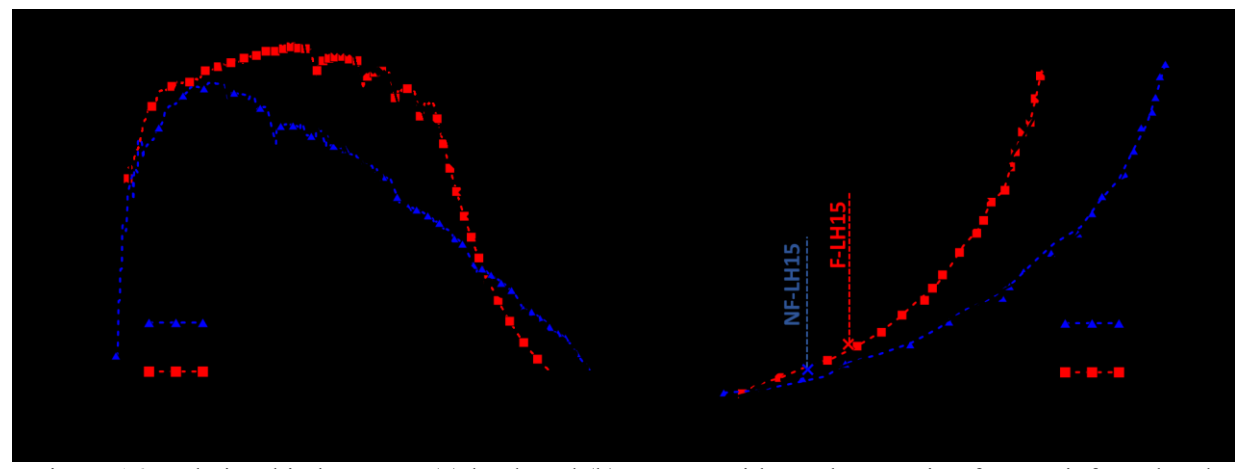


Figure 16: Relationship between: (a) load, and (b) CTOD, with crack extension for unreinforced and fiber-reinforced specimens (LH5 and LH15). The crack extension is stable to the left of the marked lines and unstable to the right, in (b). NF indicates non-fiber (unreinforced) and F indicates fiber-reinforced specimens.

3.5 Implications of layer height and fiber reinforcement on flexural and fracture properties

In an attempt to collectively examine the influence of layer height on different properties examined thus far in this paper, Figure 17 plots the normalized flexural strength and fracture properties as a function of the ratio of layer height to nozzle diameter. The normalization of the properties of the layered systems, i.e., flexural strength (σ_{flex}), fracture toughness (K_{Ic}), critical crack tip opening displacement (CTOD_c), and the strain energy release rate (G_{R-max}), is carried out with respect to those of unreinforced mold-cast specimens. Even for the fiber-reinforced specimens, the unreinforced mortar properties are used for normalization because the desired properties of the same fiber-reinforced mortar are not available at the time of preparing

this manuscript; however the benefit is that this helps evaluate the combined influence of layer height and fiber incorporation on the properties. Figure 17a shows that, for the unreinforced mortars, the flexural strength and fracture toughness are lower when the mixture is 3D printed, a possible influence of a combination of weak interfaces and the lack of external compaction. However, CTOD_c and G_{R-max} are less dependent on the method of fabrication. All the parameters show a slight decline with layer height, G_{R-max}, more so. Overall, compared to a conventionally cast specimen, the 3D printed specimen shows slightly inferior flexural and fracture properties, though changes in mixture composition and printing process could overcome some of these effects.

Figure 17b shows the normalized properties for the fiber-reinforced specimens. The flexural strengths and fracture toughness of the fiber-reinforced 3D printed specimens are generally equal to or slightly greater than those of unreinforced, mold-cast specimens – the small volume of fibers used here negates the weak interface effects. However, the normalized values of CTOD_c and G_{R-max} are much higher, showing that the use of a small amount of fiber reinforcement eliminates the negative effects of weak interfaces as far as fracture properties are concerned, and even enhances the fracture performance. Except for G_{R-max}, the other properties are less influenced by the differences in layer height, within the ranges studied in this work. From a mechanical property standpoint, it would be beneficial to use a smaller layer height for unreinforced mortars since the nozzle pressure leads to compact layers and interfaces, provided that this pressure does not result in fresh-state buildability and stability issues. However, this could result in longer printing times, which in turn could interfere with interlayer bonding, and construction productivity. If a small amount of fiber reinforcement is used, larger layer heights can be printed without attendant loss in properties, ensuring faster printing process.

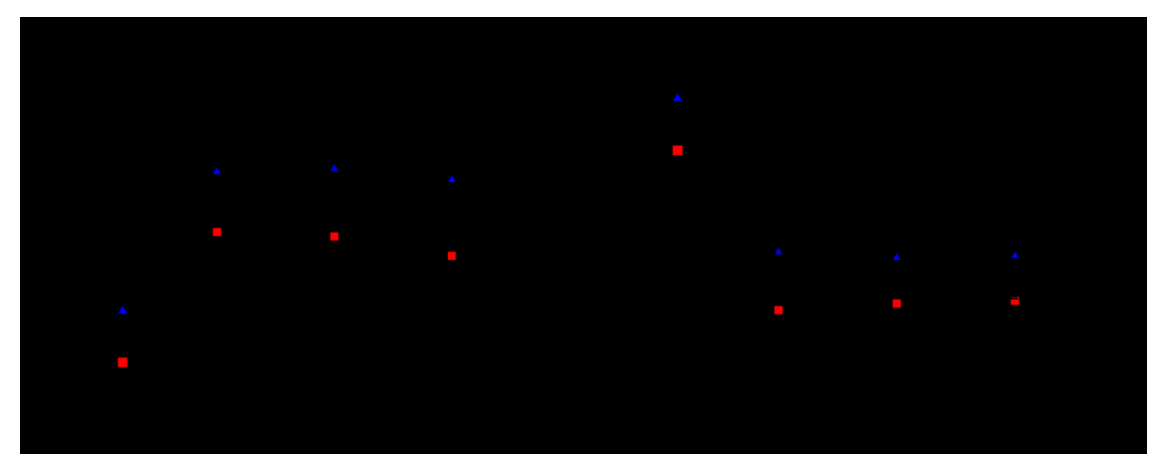


Figure 17: Normalized flexure and fracture properties as a function of layer height: (a) unreinforced, and (b) fiber-reinforced mortars. The normalization is carried out with respect to the properties of the unreinforced mold-cast mortar for both the cases.

4 Summary and Conclusions

This paper has elucidated the influence of printed layer height on the flexural and fracture properties of plain and steel fiber-reinforced 3D printed concrete beams. For the chosen mixtures satisfying extrudability and buildability criteria, layer heights corresponding to 0.25, 0.50, and 0.75 times the nozzle diameter (20 mm) were chosen, with all other printing parameters such as the print speed and layer width remaining the same. The beam specimens were subjected to four-point flexural tests and three-point notched fracture tests, accompanied by digital image correlation (DIC). The flexural strength, fracture toughness (K_{IC}), critical crack tip opening displacement (CTOD_c), and strain energy release rate (G_{R-max}) were extracted from the tests.

Microscopy revealed increasing porosity at the layer interfaces when the layer heights were larger. Better layer overlap and the larger pressing force exerted by the nozzle when printing thinner layers resulted in consolidation of the layers and the interface, resulting in reduced defects for lower layer heights. For the fiber-reinforced specimens, layer heights lower than the fiber length resulted in interfacial defects because of fiber dragging and scratching, while printing. The flexural strengths were higher for the unreinforced mortars printed with a lower layer height because of the effects of consolidation. K_{IC}, CTOD_c, and G_{R-max} also slightly decreased or remained roughly the same with increasing layer heights in the range of parameters tested, attributable to the opposing effects of increased energy dissipation due to more number of denser interfaces (for smaller layer height cases) and less number of more porous interfaces (for larger layer height cases). For mortars containing about 0.25% by volume of steel fibers, the properties were significantly higher than those of their unreinforced counterparts, demonstrating the beneficial effects of a small volume of fibers in overcoming layering-induced property deterioration. Crack propagation patterns in unreinforced mortars under four-point bending showed some crack deviation at the layer interfaces, while in the case of notched beams under three-point bending and slower loading rates, even some crack deflection into the interfaces.

The flexural and fracture property results reported here indicate that, within the parameters studied, a lower layer height is beneficial, provided that aspects relating to fresh-state buildability, exerted nozzle pressure, and the need for longer printing times, can be efficiently managed. The more compact microstructure, both in the bulk and at the interfaces, ensure better mechanical properties. Larger layer heights, even when adjacent layer overlap is specified in the print path, result in large voids which are not likely to be sealed through continuing hydration, posing potential durability issues. However, mechanical property deterioration because of larger layer heights can be overcome through the use of small amounts of fiber reinforcement.

5 Acknowledgments

The authors sincerely acknowledge support from U.S. National Science Foundation (CMMI: 1727445; OISE: 2020095) towards this this project. The contents of this paper reflect the views of the authors who are responsible for the facts and accuracy of the data presented herein, and do not necessarily reflect the views and policies of NSF, nor do the contents constitute a standard, specification or a regulation. The authors acknowledge the support from Salt River Materials Group, Omya, and Bekaert Corporation in donating the materials. We acknowledge the use of 3D printing and material characterization facilities within Laboratory for the Science of Sustainable Infrastructural Materials (LS-SIM) at Arizona State University.

6 References

- [1] A. Paolini, S. Kollmannsberger, E. Rank, Additive manufacturing in construction: A review on processes, applications, and digital planning methods, Addit. Manuf. 30 (2019) 100894. https://doi.org/10.1016/j.addma.2019.100894.
- [2] B. Khoshnevis, D. Hwang, K.-T. Yao, Z. Yeh, Mega-scale fabrication by Contour Crafting, Int. J. Ind. Syst. Eng. 1 (2006) 301–320. https://doi.org/10.1504/IJISE.2006.009791.
- [3] F. Bos, R. Wolfs, Z. Ahmed, T. Salet, Additive manufacturing of concrete in construction: potentials and challenges of 3D concrete printing, Virtual Phys. Prototyp. 11 (2016) 209–225. https://doi.org/10.1080/17452759.2016.1209867.
- [4] D. Lowke, E. Dini, A. Perrot, D. Weger, C. Gehlen, B. Dillenburger, Particle-bed 3D printing in concrete construction Possibilities and challenges, Cem. Concr. Res. 112 (2018) 50–65. https://doi.org/10.1016/j.cemconres.2018.05.018.
- [5] P. Shakor, S. Nejadi, G. Paul, J. Sanjayan, Dimensional accuracy, flowability, wettability, and porosity in inkjet 3DP for gypsum and cement mortar materials, Autom. Constr. 110 (2020) 102964. https://doi.org/10.1016/j.autcon.2019.102964.
- [6] N. Hack, I. Dressler, L. Brohmann, S. Gantner, D. Lowke, H. Kloft, Injection 3D Concrete Printing (I3DCP): Basic Principles and Case Studies, Materials. 13 (2020) 1093. https://doi.org/10.3390/ma13051093.
- [7] E. Lloret Fritschi, L. Reiter, T. Wangler, F. Gramazio, M. Kohler, R.J. Flatt, Smart Dynamic Casting: Slipforming with Flexible Formwork Inline Measurement and Control, in: HPCCIC Tromsø 2017, Norwegian Concrete Association, 2017: p. 27. https://doi.org/10.3929/ethz-b-000219663.
- [8] H. Alghamdi, S.A.O. Nair, N. Neithalath, Insights into material design, extrusion rheology, and properties of 3D-printable alkali-activated fly ash-based binders, Mater. Des. 167 (2019) 107634. https://doi.org/10.1016/j.matdes.2019.107634.
- [9] T.T. Le, S.A. Austin, S. Lim, R.A. Buswell, R. Law, A.G.F. Gibb, T. Thorpe, Hardened properties of high-performance printing concrete, Cem. Concr. Res. 42 (2012) 558–566. https://doi.org/10.1016/j.cemconres.2011.12.003.
- [10] A.R. Arunothayan, B. Nematollahi, R. Ranade, S.H. Bong, J. Sanjayan, Development of 3D-printable ultra-high performance fiber-reinforced concrete for digital construction, Constr. Build. Mater. 257 (2020) 119546. https://doi.org/10.1016/j.conbuildmat.2020.119546.
- [11] B. Nematollahi, M. Xia, S.H. Bong, J. Sanjayan, Hardened Properties of 3D Printable 'One-Part' Geopolymer for Construction Applications, in: T. Wangler, R.J. Flatt (Eds.), First RILEM Int. Conf. Concr. Digit. Fabr. Digit. Concr. 2018, Springer International Publishing, Cham, 2019: pp. 190–199. https://doi.org/10.1007/978-3-319-99519-9 17.

- [12] B. Panda, S.C. Paul, L.J. Hui, Y.W.D. Tay, M.J. Tan, Additive manufacturing of geopolymer for sustainable built environment, J. Clean. Prod. 167 (2017) 281–288. https://doi.org/10.1016/j.jclepro.2017.08.165.
- [13] H. Alghamdi, N. Neithalath, Synthesis and characterization of 3D-printable geopolymeric foams for thermally efficient building envelope materials, Cem. Concr. Compos. 104 (2019) 103377. https://doi.org/10.1016/j.cemconcomp.2019.103377.
- [14] N. Roussel, Rheological requirements for printable concretes, Cem. Concr. Res. 112 (2018) 76–85. https://doi.org/10.1016/j.cemconres.2018.04.005.
- [15] S.A.O. Nair, S. Panda, M. Santhanam, G. Sant, N. Neithalath, A critical examination of the influence of material characteristics and extruder geometry on 3D printing of cementitious binders, Cem. Concr. Compos. 112 (2020) 103671. https://doi.org/10.1016/j.cemconcomp.2020.103671.
- [16] A. Kazemian, X. Yuan, E. Cochran, B. Khoshnevis, Cementitious materials for construction-scale 3D printing: Laboratory testing of fresh printing mixture, Constr. Build. Mater. 145 (2017) 639–647. https://doi.org/10.1016/j.conbuildmat.2017.04.015.
- [17] B. Panda, C. Unluer, M.J. Tan, Extrusion and rheology characterization of geopolymer nanocomposites used in 3D printing, Compos. Part B Eng. 176 (2019) 107290. https://doi.org/10.1016/j.compositesb.2019.107290.
- [18] L. Reiter, T. Wangler, N. Roussel, R.J. Flatt, The role of early age structural build-up in digital fabrication with concrete, Cem. Concr. Res. 112 (2018) 86–95. https://doi.org/10.1016/j.cemconres.2018.05.011.
- [19] G. Ma, N.M. Salman, L. Wang, F. Wang, A novel additive mortar leveraging internal curing for enhancing interlayer bonding of cementitious composite for 3D printing, Constr. Build. Mater. 244 (2020) 118305. https://doi.org/10.1016/j.conbuildmat.2020.118305.
- [20] J. Yu, C.K.Y. Leung, Impact of 3D Printing Direction on Mechanical Performance of Strain-Hardening Cementitious Composite (SHCC), in: T. Wangler, R.J. Flatt (Eds.), First RILEM Int. Conf. Concr. Digit. Fabr. Digit. Concr. 2018, Springer International Publishing, Cham, 2019: pp. 255–265. https://doi.org/10.1007/978-3-319-99519-9 24.
- [21] M. Hambach, D. Volkmer, Properties of 3D-printed fiber-reinforced Portland cement paste, Cem. Concr. Compos. 79 (2017) 62–70. https://doi.org/10.1016/j.cemconcomp.2017.02.001.
- [22] A.V. Rahul, M. Santhanam, H. Meena, Z. Ghani, Mechanical characterization of 3D printable concrete, Constr. Build. Mater. 227 (2019) 116710. https://doi.org/10.1016/j.conbuildmat.2019.116710.
- [23] S. Al-Qutaifi, A. Nazari, A. Bagheri, Mechanical properties of layered geopolymer structures applicable in concrete 3D-printing, Constr. Build. Mater. 176 (2018) 690–699. https://doi.org/10.1016/j.conbuildmat.2018.04.195.
- [24] Z. Geng, W. She, W. Zuo, K. Lyu, H. Pan, Y. Zhang, C. Miao, Layer-interface properties in 3D printed concrete: Dual hierarchical structure and micromechanical characterization, Cem. Concr. Res. 138 (2020) 106220. https://doi.org/10.1016/j.cemconres.2020.106220.
- [25] B. Zareiyan, B. Khoshnevis, Effects of interlocking on interlayer adhesion and strength of structures in 3D printing of concrete, Autom. Constr. 83 (2017) 212–221. https://doi.org/10.1016/j.autcon.2017.08.019.
- [26] Z. Li, L. Wang, G. Ma, Method for the Enhancement of Buildability and Bending Resistance of 3D Printable Tailing Mortar, Int. J. Concr. Struct. Mater. 12 (2018) 37. https://doi.org/10.1186/s40069-018-0269-0.
- [27] B. Panda, S.C. Paul, N.A.N. Mohamed, Y.W.D. Tay, M.J. Tan, Measurement of tensile bond strength of 3D printed geopolymer mortar, Measurement. 113 (2018) 108–116. https://doi.org/10.1016/j.measurement.2017.08.051.
- [28] R.J.M. Wolfs, F.P. Bos, T.A.M. Salet, Hardened properties of 3D printed concrete: The influence of process parameters on interlayer adhesion, Cem. Concr. Res. 119 (2019) 132–140. https://doi.org/10.1016/j.cemconres.2019.02.017.

- [29] V.N. Nerella, S. Hempel, V. Mechtcherine, Effects of layer-interface properties on mechanical performance of concrete elements produced by extrusion-based 3D-printing, Constr. Build. Mater. 205 (2019) 586–601. https://doi.org/10.1016/j.conbuildmat.2019.01.235.
- [30] Y. Chen, K. Jansen, H. Zhang, C. Romero Rodriguez, Y. Gan, O. Çopuroğlu, E. Schlangen, Effect of printing parameters on interlayer bond strength of 3D printed limestone-calcined clay-based cementitious materials: An experimental and numerical study, Constr. Build. Mater. 262 (2020) 120094. https://doi.org/10.1016/j.conbuildmat.2020.120094.
- [31] T. Wangler, E. Lloret, L. Reiter, N. Hack, F. Gramazio, M. Kohler, M. Bernhard, B. Dillenburger, J. Buchli, N. Roussel, Digital concrete: opportunities and challenges, RILEM Tech. Lett. 1 (2016) 67–75.
- [32] T. Marchment, J. Sanjayan, M. Xia, Method of enhancing interlayer bond strength in construction scale 3D printing with mortar by effective bond area amplification, Mater. Des. 169 (2019) 107684. https://doi.org/10.1016/j.matdes.2019.107684.
- [33] S.A. Nair, H. Alghamdi, A. Arora, I. Mehdipour, G. Sant, N. Neithalath, Linking fresh paste microstructure, rheology and extrusion characteristics of cementitious binders for 3D printing, J. Am. Ceram. Soc. 102 (2019) 3951–3964.
- [34] B. Panda, S. Chandra Paul, M. Jen Tan, Anisotropic mechanical performance of 3D printed fiber reinforced sustainable construction material, Mater. Lett. 209 (2017) 146–149. https://doi.org/10.1016/j.matlet.2017.07.123.
- [35] F.P. Bos, E. Bosco, T.A.M. Salet, Ductility of 3D printed concrete reinforced with short straight steel fibers, Virtual Phys. Prototyp. 14 (2019) 160–174. https://doi.org/10.1080/17452759.2018.1548069.
- [36] G. Ma, Z. Li, L. Wang, F. Wang, J. Sanjayan, Mechanical anisotropy of aligned fiber reinforced composite for extrusion-based 3D printing, Constr. Build. Mater. 202 (2019) 770–783. https://doi.org/10.1016/j.conbuildmat.2019.01.008.
- [37] ASTM International, C78/C78M-18 Standard test method for flexural strength of concrete (using simple beam with third-point loading), ASTM International, West Conshohocken, PA, 2018. https://doi.org/10.1520/C0078 C0078M-18.
- [38] ASTM International, C293/C293M-16 Standard test method for flexural strength of concrete (Using simple beam with center-point loading), ASTM International, West Conshohocken, PA, 2016. https://doi.org/10.1520/C0293 C0293M-16.
- [39] Y.S. Jenq, S.P. Shah, A Fracture toughness criterion for concrete, Eng. Fract. Mech. 21 (1985) 1055–1069. https://doi.org/10.1016/0013-7944(85)90009-8.
- [40] S.P. Shah, Determination of fracture parameters (K Ic s and CTODc) of plain concrete using three-point bend tests, Mater. Struct. 23 (1990) 457–460. https://doi.org/10.1007/BF02472029.
- [41] S. Das, M. Aguayo, V. Dey, R. Kachala, B. Mobasher, G. Sant, N. Neithalath, The fracture response of blended formulations containing limestone powder: Evaluations using two-parameter fracture model and digital image correlation, Cem. Concr. Compos. 53 (2014) 316–326. https://doi.org/10.1016/j.cemconcomp.2014.07.018.
- [42] Z. Zhao, S.H. Kwon, S.P. Shah, Effect of specimen size on fracture energy and softening curve of concrete: Part I. Experiments and fracture energy, Cem. Concr. Res. 38 (2008) 1049–1060. https://doi.org/10.1016/j.cemconres.2008.03.017.
- [43] M. Wecharatana, S.P. Shah, A model for predicting fracture resistance of fiber reinforced concrete, Cem. Concr. Res. 13 (1983) 819–829. https://doi.org/10.1016/0008-8846(83)90083-2.
- [44] Effect of Ground Copper Slag on Strength and Toughness of Cementitious Mixes, ACI Mater. J. 96 (1999) 68–73. https://doi.org/10.14359/430.
- [45] S. Das, A. Kizilkanat, N. Neithalath, Crack propagation and strain localization in metallic particulate-reinforced cementitious mortars, Mater. Des. 79 (2015) 15–25. https://doi.org/10.1016/j.matdes.2015.04.038.
- [46] S. Das, D. Stone, B. Mobasher, N. Neithalath, Strain energy and process zone based fracture characterization of a novel iron carbonate binding material, Eng. Fract. Mech. 156 (2016) 1–15. https://doi.org/10.1016/j.engfracmech.2016.01.024.

- [47] D. Heras Murcia, M. Genedy, M.M. Reda Taha, Examining the significance of infill printing pattern on the anisotropy of 3D printed concrete, Constr. Build. Mater. 262 (2020) 120559. https://doi.org/10.1016/j.conbuildmat.2020.120559.
- [48] G. Ma, Z. Li, L. Wang, Printable properties of cementitious material containing copper tailings for extrusion based 3D printing, Constr. Build. Mater. 162 (2018) 613–627. https://doi.org/10.1016/j.conbuildmat.2017.12.051.
- [49] P. Carneau, R. Mesnil, N. Ducoulombier, N. Roussel, O. Baverel, Characterisation of the Layer Pressing Strategy for Concrete 3D Printing, in: RILEM Int. Conf. Concr. Digit. Fabr., Springer, 2020: pp. 185–195. https://doi.org/10.1007/978-3-030-49916-7 19.
- [50] S. Nayak, N.M.A. Krishnan, S. Das, Fracture response of metallic particulate-reinforced cementitious composites: Insights from experiments and multiscale numerical simulations, Cem. Concr. Compos. 97 (2019) 154–165. https://doi.org/10.1016/j.cemconcomp.2018.12.026.
- [51] S. Das, A. Hendrix, D. Stone, N. Neithalath, Flexural fracture response of a novel iron carbonate matrix Glass fiber composite and its comparison to Portland cement-based composites, Constr. Build. Mater. 93 (2015) 360–370. https://doi.org/10.1016/j.conbuildmat.2015.06.011.
- [52] B. Mobasher, H. Stang, S.P. Shah, Microcracking in fiber reinforced concrete, Cem. Concr. Res. 20 (1990) 665–676. https://doi.org/10.1016/0008-8846(90)90001-E.
- [53] M.T. Tilbrook, K. Rozenburg, E.D. Steffler, L. Rutgers, M. Hoffman, Crack propagation paths in layered, graded composites, Compos. Part B Eng. 37 (2006) 490–498. https://doi.org/10.1016/j.compositesb.2006.02.012.
- [54] S. Xu, H.W. Reinhardt, A simplified method for determining double-K fracture parameters for three-point bending tests, Int. J. Fract. 104 (2000) 181–209. https://doi.org/10.1023/A:1007676716549.